Eur. Phys. J. A **24**, 237–247 (2005)
DOI 10.1140/epja/i2004-10143-4

THE EUROPEAN PHYSICAL JOURNAL A

Study of ^{19}Na at SPIRAL

F. de Oliveira Santos[1,a], P. Himpe[1,2], M. Lewitowicz[1], I. Stefan[1,8], N. Smirnova[2], N.L. Achouri[3], J.C. Angélique[3], C. Angulo[4], L. Axelsson[14], D. Baiborodin[6], F. Becker[1], M. Bellegui[5], E. Berthoumieux[7], B. Blank[12], C. Borcea[8], A. Cassimi[13], J.M. Daugas[9,1], G. de France[1], F. Dembinski[1], C.E. Demonchy[1], Z. Dlouhy[6], P. Dolégiéviez[1], C. Donzaud[5], G. Georgiev[1], L. Giot[1], S. Grévy[3], D. Guillemaud Mueller[5], V. Lapoux[7], E. Liénard[3], M.J. Lopez Jimenez[1,9], K. Markenroth[14], I. Matea[1], W. Mittig[1], F. Negoita[8], G. Neyens[2], N. Orr[3], F. Pougheon[5], P. Roussel Chomaz[1], M.G. Saint Laurent[1], F. Sarazin[1,10], H. Savajols[1], M. Sawicka[1,11], O. Sorlin[5], M. Stanoiu[1], C. Stodel[1], G. Thiamova[6], D. Verney[1], and A.C.C. Villari[1]

[1] Grand Accélérateur National d'Ions Lourds, B.P. 5027, F-14076 Caen Cedex, France
[2] Instituut voor Kern- en Stralingsfysica, University of Leuven, Celestijnenlaan 200 D, B-3001 Leuven, Belgium
[3] Laboratoire de Physique Corpusculaire, IN2P3-CNRS, ISMRA et Université de Caen, F-14050 Caen, France
[4] Centre de Recherches du Cyclotron, UCL, 2 chemin du cyclotron, B-1348 Louvain-la-Neuve, Belgium
[5] Institut de Physique Nucléaire, IN2P3-CNRS, F-91406 Orsay, France
[6] Nuclear Physics Institute ASCR, CZ-25068 Rez, Czech Republic
[7] CEA Saclay, DSM/DAPNIA/SPHN, F-91191 Gif-sur-Yvette, France
[8] Institute of Atomic Physics, P.O. Box MG6, Bucharest-Margurele, Romania
[9] CEA/DIF/DPTA/PN, B.P. 12, 91680 Bruyères le Châtel, France
[10] TRIUMF, 4004 Wesbrook Mall, Vancouver, British Columbia, V6T 2A3, Canada
[11] Institute of Experimental Physics, University of Warsaw, Hoza 69, PL-00-681 Warsaw, Poland
[12] Centre d'Etudes Nucléaires de Bordeaux-Gradignan, Le Haut-Vigneau, B.P. 120, F-33175 Gradignan Cedex, France
[13] CIRIL, Rue Claude Bloch, B.P. 5133, F-14070 Caen Cedex, France
[14] Experimentell fysik, Chalmers Tekniska Högskola och Göteborgs Universitet, S-412 96 Göteborg, Sweden

Received: 25 October 2004 / Revised version: 3 March 2005 /
Published online: 13 April 2005 –
Communicated by W. Henning

Abstract. The excitation function for the elastic-scattering reaction p(^{18}Ne, p)^{18}Ne was measured with the first radioactive beam from the SPIRAL facility at the GANIL laboratory and with a solid cryogenic hydrogen target. Several broad resonances have been observed, corresponding to new excited states in the unbound nucleus ^{19}Na. In addition, two-proton emission events have been identified and are discussed.

PACS. 27.20.+n $6 \leq A \leq 19$ – 25.40.Cm Elastic proton scattering – 25.40.Ep Inelastic proton scattering – 25.60.-t Reactions induced by unstable nuclei

1 Introduction

Sodium isotopes have been produced with a wide range of neutron numbers, from the most neutron-rich isotope ^{37}Na ($N = 26$), identified for the first time in recent experiments performed at RIKEN [1] and at GANIL [2] with the new facility LISE 2000, to the most neutron-deficient isotope ^{18}Na ($N = 7$), lying two steps beyond the proton drip line [3].

Our knowledge about ^{19}Na is very limited. The first observation of ^{19}Na was performed in 1969 by Cerny *et al.* [4] using the reaction ^{24}Mg(p, ^{6}He)^{19}Na. The differential cross-section for this reaction was $\sim$ 100 nb/sr and the resolution was about 200 keV. One peak was observed at the mass excess of 12.974 ± 0.070 MeV, a value quite close to the value of 12.90 MeV predicted with the Isobaric Mass Multiplet Equation (IMME). This measured mass implied that it is unbound against one proton emission. In another experiment, Benenson *et al.* [5] used the reaction ^{24}Mg(^{3}He, ^{8}Li)^{19}Na to study this nucleus. Compared to the previous reaction, the differential cross-section was about 3 times higher and the energy resolution was about 40 keV. Two peaks were observed in the ^{8}Li energy spectrum and attributed to the ground and first-excited states. A more precise value for the mass of the ground state was obtained, which was only $E_R = 320 \pm 12$ keV above the proton emission threshold. The first-excited state was measured at the excitation energy $E_x = 120 \pm 10$ keV, but it was observed as a small

[a] e-mail: oliveira@ganil.fr

peak in the tail of the ground-state peak. This result is consistent with the known properties of the other $T = 3/2$ isobaric analog states [6], where the first-excited state always lies very close to the ground state (in ^{19}O the energy difference is 96 keV, in ^{19}F it is 121 keV and in ^{19}Ne it is 85 keV). In another experiment performed at GANIL and based on the invariant-mass method, Zerguerras *et al.* [3] were able to measure the mass spectrum corresponding to ^{19}Na. They could see only one peak, at the position of $E_R = 480 \pm 50$ keV. Regrettably, in all these measurements the intensity for the feeding of the different states was not discussed. It is surprising that none of the other excited states was observed.

Recently, the second-excited state was seen in a precise resonant-elastic-scattering measurement performed by Angulo *et al.* [7]. In this case a ^{18}Ne beam impinged onto a (0.5 mg/cm^2) polyethylene target. A new state was observed at $E_R = 1066 \pm 2$ keV, having $\Gamma = 101 \pm 3$ keV and $J^\pi = \frac{1}{2}^+$. This state corresponds to the known second-excited state in the mirror nucleus ^{19}O. It is 725 keV below from its analog in ^{19}O.

We report here the results of a new study. We measured the resonant elastic scattering of a ^{18}Ne beam on a thick solid cryogenic hydrogen target. This experiment was the first experiment performed with a radioactive beam from the SPIRAL facility at GANIL. In the following sections 2-4 we present the experimental part of this measurement. The analysis of the excitation function is presented in sects. 5-7. Results of calculations using a potential model and the shell model are also presented, and compared with the measured levels and with the known states in the mirror nucleus ^{19}O. And, finally, two-proton events observed in the same experiment are analyzed and discussed.

2 Experimental setup

In order to investigate the structure of the ^{19}Na isotope, we have measured the excitation function of the elastic-scattering reaction in inverse kinematics p(^{18}Ne, p)^{18}Ne . The basic idea of the measurement is presented in the refs. [7–11] and references therein. We have performed the experiment with a target thick enough to stop the beam inside it. The idea of using this kind of target for elastic scattering has been developed successfully in several experiments [12–14]. The scattered proton can escape the target because of its smaller energy loss, and can be detected at forward angles in the laboratory frame. Therefore, the thick target makes it possible to obtain a complete and continuous excitation function over a wide range of energies, by detecting the scattered protons and measuring their energies, without changing the energy of the incident beam. As measured, for example, by Axelsson *et al.* [12], the final energy resolution is better than 50 keV in the center-of-mass frame, generally good enough to study states with large widths. The disadvantages of using a thick target are discussed later.

The elastic-scattering measurement was performed at GANIL with a radioactive beam produced by the new SPIRAL (Système de Production d'Ions RAdioactifs en Ligne) facility [15,16]. The ^{18}Ne beam was produced through the projectile fragmentation of a ^{20}Ne primary beam at 95 A MeV on a carbon target, located at the new underground production cave of SPIRAL. For this first experiment, a maximum primary beam intensity of ~ 0.20 pμA has been used (in order to limit the irradiation of the production ensemble). The radioactive atoms released from the carbon target —heated to 2000 K— were ionized by the Nanogan-3 ECR ion source to the charge state 4+. The beam was accelerated by the new compact cyclotron CIME (Cyclotron d'Ions à Moyenne Energie) up to an energy of 7.2 A MeV. The beam was contaminated by 15% of ^{18}O and a very small amount ($< 1\%$) of ^{18}F. The efficiency of the overall production system can be disentangled in the following way. More than 90% of the produced atoms diffuse out of the target and arrive in the ECR ion source. About 15% of these atoms are extracted in the charge state 4+. The transmission of the low-energy separator, corresponding to the first half of the injection line of CIME, was of the order of 50%, while the transmission of the CIME accelerator including the beam pulsing and beam extraction was also 50%. The observed efficiencies were close to the expected ones. The present design of the carbon target allows to increase the primary beam intensity up to 1 pμA, which will correspond to 10^7 particles per second of ^{18}Ne. The excellent stability and reproducibility of the whole production and acceleration system of SPIRAL should be underlined. During the experiment, one could easily change the tuning of the cyclotron from ^{18}O, used for calibrations, to ^{18}Ne in about 15 minutes. To get rid of the contamination we have used the LISE magnetic spectrometer as a separator. A thin carbon stripper foil (40 μg/cm^2) was placed at the target position of the spectrometer to select the 10+ charge state of the beam, yielding a pure ^{18}Ne^{10+} beam with a mean intensity of 2.5 10^5 pps. During the whole experiment, the beam intensity was measured and monitored by using a multi-channel plate detector placed in front of the target.

A pure 1 mm thick hydrogen target was chosen to be used in this experiment for two reasons. First, the use of compound targets (*e.g.* $(CH_2)_n$) introduces other elements (*e.g.* carbon) in which new reactions can occur and may disturb the measurement. We have performed several measurements with this kind of target and we have observed that the carbon contributes a non-negligible continuous background at this incident energy. Second, the use of a pure hydrogen target maximizes the counting rate because the highest stoechiometric ratio leads to the highest effective target thickness. The main requirements imposed for the development of solid cryogenic targets usable under vacuum are: low thickness, very thin windows, and uniform thickness and density. A special cryogenic system has been designed to make this target [17]. Cryogenic target systems have already been designed in various laboratories, particularly by directly condensing H_2 gas to make the target. In the system developed at GANIL, we have opted for a transition to the liquid phase (16.2 K - 230 mbar) before progressive solidification of the hydrogen

($T < 13.9$ K). Liquid helium has been used as a cold source at 4 K and the growth of the hydrogen crystal has been imposed by the temperature gradient in the metal frame supporting the target. The target was made using a metal frame to which mylar windows (6 μm) were glued. A stack of frames has formed a H_2 target cell with a He cell on either side of the target. During the target production phase, equivalent pressure has been maintained on either side of the target windows. Once the target was formed, the helium gas was evacuated. The target was placed in the experiment vessel during nearly a week ($P \sim 20$ μW on the target) and temperature was kept below 9 K.

The scattered protons escaped from the cryogenic target and were detected in a telescope of 3 silicon detectors 50×50 mm in size. We used a 150 μm ΔE detector, a 1 mm double-sided strip detector and a 3.5 mm thick Si(Li) detector. A large total thickness of the telescope was chosen in order to cover the full proton energy interval. The ΔE detector was placed 317 mm behind the target in order to decrease the counting rate due to the β-rays from the decay of the beam particles. The second silicon detector was placed just behind the first one. The angular acceptance of this detector was $\pm 4.5°$ (in the laboratory frame). Due to geometrical constraints the Si(Li) detector was placed farther away from this ensemble, 495 mm from the target, corresponding to a calculated solid angle of $\mathrm{d}\Omega_{\mathrm{lab}} = 10$ msr.

3 Calibration with p(^{18}O, p)^{18}O

Two corrections must be applied to the data to obtain the excitation function. A first correction is applied for the energy loss of the protons inside the hydrogen target. We have used the energy losses calculated with the program SRIM [18] to determine this correction. In fig. 1 we can observe in (a) that the energy loss changes slowly over the full range of the proton energies of interest (between 2.5 MeV and 25 MeV in the laboratory frame). The second correction shown in (b) has to be applied for normalization. The effective target thickness at a certain energy depends on the energy loss of the incident ions at this energy. This effect explains why it is interesting to use a pure hydrogen target. In that case, we obtain the lowest energy loss and the highest proton density, which both increase the counting rate. We can observe that the counting rate (per barns per steradian in the center-of-mass frame per 10^9 incident ions per keV in the laboratory frame) increases with energy, we are more sensitive to higher energies, which compensates for the usually lower cross-section at those energies.

We performed a measurement with a stable beam to determine the mean target thickness and to evaluate the uniformity of the cryogenic target. This measurement was accomplished with an ^{18}O beam, produced at the same energy as ^{18}Ne. The energy of the incident beam (7.2 A MeV) was chosen to stop the ^{18}O beam at the downstream edge of the target. The final result is shown in fig. 2. This spectrum was measured in 2.8 hours, with a mean beam intensity of 10^6 pps.

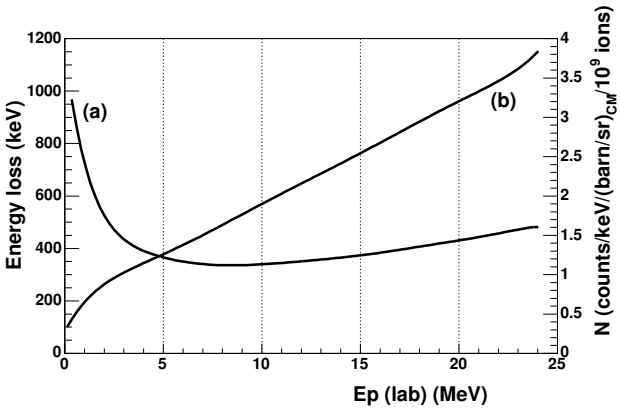

Fig. 1. The energy loss (left axis in keV) of the protons inside the hydrogen target is plotted in curve (a) *versus* the proton energy (in MeV) in the laboratory frame. Moreover, the number of counts N (per barns per steradian in the center-of-mass frame per 10^9 incident ions per keV in the laboratory frame) is plotted (curve (b), right axis) as a function of the detected proton energy.

From the measurement we were able to perform two comparisons:

- A part of our measured excitation function was already measured by Orihara *et al.* [19] in a very precise direct kinematics experiment (energy resolution $\sim$ 2.5 keV). The related data are shown in the insert of fig. 2 as a dotted line. The excitation function was measured at an angle of $\Theta_{\mathrm{CM}} = 168.7°$, different from our value $\Theta_{\mathrm{CM}} = 180°$, but the difference is small enough to make this comparison valid. There is a good agreement in energy and in normalization. Through the comparison, used as a calibration measurement, it was possible to determine precisely the mean target thickness of 1050 ± 20 μm (using a constant density of 88.5 mg/cm^3). Moreover, we measured an energy resolution of 30 ± 10 keV, constant in this range of energy. This value is in good agreement with those obtained in similar experiments [12,14] using homogeneous gas targets. Using this value of the energy resolution, we have determined a standard deviation of 70 μm for the target thickness, demonstrating the good quality of the cryogenic target used here. Furthermore, the absolute normalization of the data corresponds to $\mathrm{d}\Omega_{\mathrm{lab}} = 11 \pm 1$ msr (in the configuration using the Si(Li) detector).
- The properties of the ^{19}F (^{18}O + p) states lying at excitation energies $8 \leq E_x \leq 15$ MeV are quite well known. We have compared our measurement with a R-matrix calculation performed using all known states (37 in total) (from [19,6]) of ^{19}F in the measured energy range. The R-matrix calculation has been performed with the code ANARKI [20]. Figure 2 shows the result of this calculation folded with the experimental energy resolution as a continuous curve. We observe an overall good agreement, both in normalization and in energy. No extra peak is visible in the spectrum. The differences observed

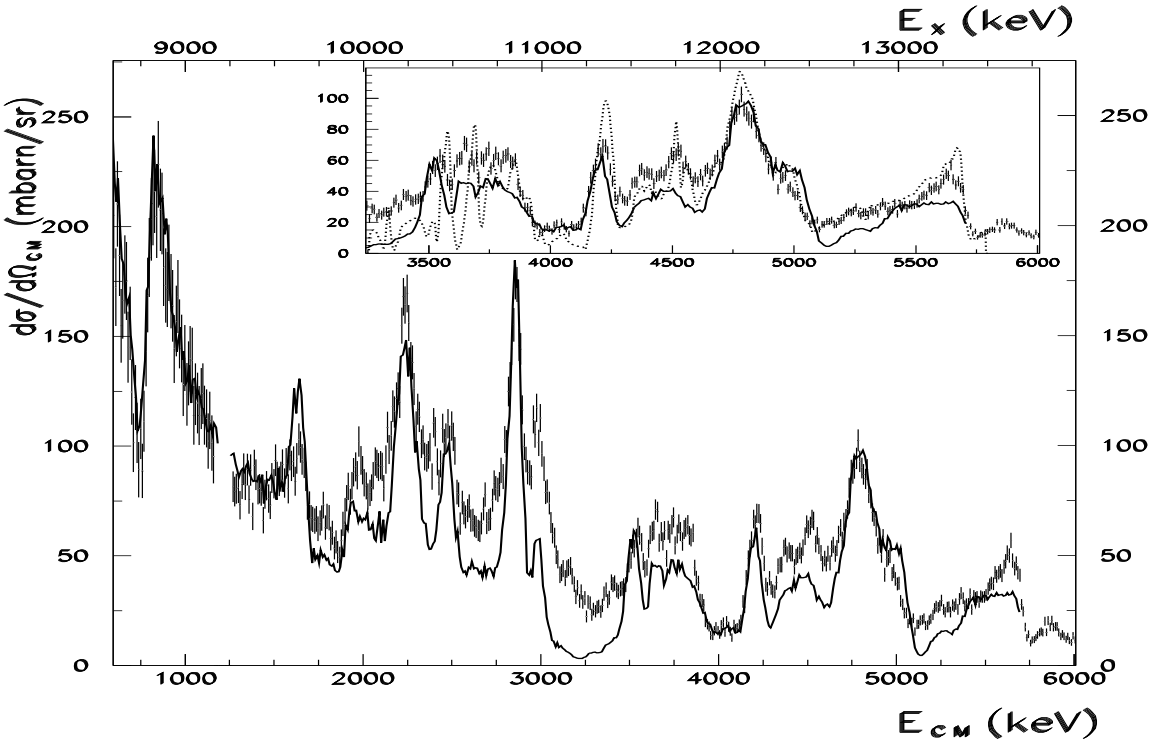

Fig. 2. The excitation function for the elastic-scattering reaction p(^{18}O, p)^{18}O measured at $\Theta_{\rm CM} = 180^{\circ}$. The reconstructed differential cross-section is plotted as a function of the center-of-mass energy $E_{\rm CM}$ (lower axis) and the excitation energy E_x in ^{19}F (upper axis). The error bars are statistical. The continuous curve represents a R-matrix calculation using the known properties of 37 states in ^{19}F. Differences between the experimental data and the calculated excitation function could arise due to the lack of knowledge of the widths of some states. The experimental energy resolution was measured to be ~ 30 keV. Insert: a zoom of the high-energy part of the spectrum is shown, the continuous curve corresponds to the R-matrix calculation, the dotted curve represents the excitation function from Orihara *et al.* [19] measured at $\Theta_{\rm CM} = 168.7^{\circ}$.

between the calculation and the measurement are certainly due to the uncertainties in the known and unknown properties of the excited states in ^{19}F. The low-energy part of the spectrum was calibrated using the results of the R-matrix calculation. In fig. 2, at an $E_{\rm CM} \approx 1.1$ MeV there is an energy gap of ≈ 200 keV without data. This gap results from selection conditions. The protons with energies higher than this energy gap are identified and selected using a standard contour in a ΔE-E plot. For the lower-energy part of the spectrum, firstly we have applied a time-of-flight selection to identify the protons. Secondly, to select the particles stopped in the first detector we applied a low-energy threshold on the second detector.

In conclusion, this calibration measurement allowed us to extract different parameters characterizing our experimental setup (energy calibration, normalization, target thickness, resolution etc.). The measured values for these parameters are very close to those expected or calculated.

4 Measurement of p(^{18}Ne, p)^{18}Ne

Figure 3 shows the excitation function for the elastic scattering of a radioactive ^{18}Ne beam on the proton target. It represents a 38 hour measurement. For the analysis of the data, we have used the measured values of the experimental parameters deduced from the calibration measurement performed with the ^{18}O beam. The ^{18}Ne and ^{18}O nuclei have different range in the proton target, resulting in different energy resolutions. In the center-of-mass frame the energy resolution is calculated to be only 2 keV worse with ^{18}Ne. In fig. 3 only a few broad resonances can be seen, labelled from A to F. The compound nucleus ^{19}Na is populated at lower excitation energies than in the case of ^{19}F, which correspond to a region of a lower density of states.

5 Analysis and discussion

The characteristic shape of the first peak A in fig. 3 suggests its spin and parity assignment $J^{\pi} = \frac{1}{2}^{+}$. For that state we obtained $E_{\rm CM} = 1076 \pm 6$ keV and $\Gamma = 80 \pm 20$ keV. These values are in good agreement with the already known properties of the second-excited state in ^{19}Na, previously measured at $E_{\rm CM} = 1066 \pm 2$ keV with a width $\Gamma = 101 \pm 3$ keV [7]. It is very interesting to compare this level with the known levels in ^{19}O, since the position of the excited states and the spectroscopic factors should be nearly identical for mirror nuclei. This level is

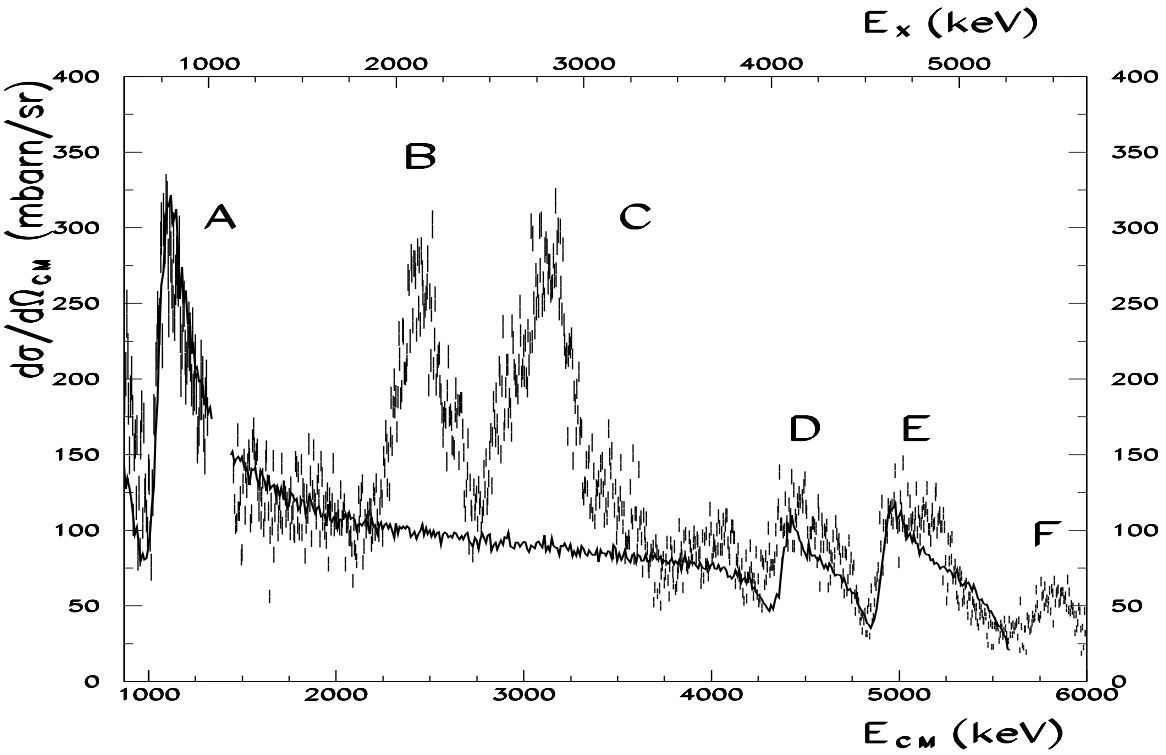

Fig. 3. The reconstructed differential cross-section ($\Theta_{\rm CM} = 180^\circ$) for the elastic-scattering reaction p(^{18}Ne, p)^{18}Ne is shown as a function of the center-of-mass energy $E_{\rm CM}$ (lower axis) and the excitation energy E_x in ^{19}Na (upper axis). The labels correspond to the peaks described in the text. The continuous line represents a R-matrix calculation when the properties of four states of ^{19}Na are taken into account (see text). This figure corresponds to a measurement with a total of $3.4 \cdot 10^{10}$ incident ^{18}Ne nuclei.

positioned at an excitation energy $E_x = 746 \pm 14$ keV in ^{19}Na, which only matches in the mirror nucleus with the known $\frac{1}{2}^+$ state at a position of $E_x = 1471.7 \pm 0.4$ keV. This means that the corresponding state in ^{19}Na is lowered by 725 ± 15 keV.

To study the origin of this energy shift we have performed calculations using a potential model. The analog state in ^{19}O was built with a model of one neutron in the potential of an ^{18}O core. This model is clearly a good approximation when the spectroscopic factor θ^2 for this configuration is close to 1, which is the case in the mirror nucleus. In a first step, we have fitted the depth of a Wood-Saxon well to reproduce the experimental neutron separation energy. In a second step, we have used the same potential in addition to the Coulomb interaction for the mirror system of one proton and a ^{18}Ne core. The calculation shows an energy shift between analog states. The largest shift is observed for the s-orbital, which corresponds to the $J^\pi = \frac{1}{2}^+$ assignment of the state. In this case, we calculated an energy shift of 749 keV, a value very close to the experimental one. We performed a shell model calculation for that state (using the code and parameters presented hereafter), which predicts a spectroscopic factor $\theta^2 = 0.83$. This calculated value of the spectroscopic factor, using our potential model, is equivalent to a width $\Gamma = 96$ keV, again in agreement with the experimental value. In conclusion, this state can be mainly described by the shell model configuration $\pi(1d5/2)^2(2s1/2)^1$ and the origin of the energy shift is mainly due to the Coulomb interaction.

The intense and broad ($\Gamma \approx 300$ keV) peak B at an energy $E_{\rm CM} \approx 2.4$ MeV corresponds to an excitation energy $E_x \approx 2.1$ MeV. Surprisingly, it does not match any known state in the mirror nucleus. There are two known states in ^{19}O at energies $E_x = 2.3715$ MeV and $E_x = 2.7790$ MeV. However, these states cannot match because they are assigned with spins $J^\pi = \frac{9}{2}^+$ and $\frac{7}{2}^+$ implying an angular momentum $\ell = 4$. This high value of the angular momentum is excluded in our experiment because it corresponds to a very narrow width. There are also two other known states in the mirror nucleus, positioned at excitation energies $E_x = 3.0671$ MeV and $E_x = 3.1535$ MeV. The spin assignments are $\frac{3}{2}^+$ and $\frac{5}{2}^+$, which means the angular-momentum number is $\ell = 2$. Those states are also excluded because the Coulomb energy shift cannot be so large as to explain the difference in energy.

The broad ($\Gamma \approx 500$ keV) peak C is positioned at an energy $E_{\rm CM} \approx 3.1$ MeV, corresponding to an excitation energy $E_x \approx 2.8$ MeV. The intensity and the shape of this peak are very similar to those of peak B. There is also no known analog state in the mirror nucleus which could correspond to this peak.

In order to understand the origin of peaks B and C, we have performed shell model calculations, since:

– All states are not known experimentally in the mirror partner ^{19}O. Performing shell model calculations gives the possibility of predicting the positions of states in ^{19}Na.
– Calculations give the possibility to predict the spectroscopic factors θ^2, *i.e.* the superposition probabilities between the entrance channel ^{18}Ne + p and the different states in the compound nucleus ^{19}Na*, and also between the different states in ^{19}Na* and the different inelastic-scattering channels ^{18}Ne* + p. This allows the calculation of the widths for elastic and inelastic scattering.

For the nuclei with $A = 19$ and $T = 3/2$ we have performed a shell model calculation in the *sps-dpf* space and with the WBT [21] interaction. This calculation has been carried out with the shell model code Oxbash [22]. We have allowed 0 and 1 $\hbar\omega$ excitations, which have permitted the existence of low-lying negative-parity states. We have calculated all states up to $E_x = 5.5$ MeV, and all elastic-scattering channels up to the angular-momentum number $\ell = 3$. We have also calculated all inelastic-scattering channels on the first-excited state in ^{18}Ne (2^+, $E_x = 1887$ keV [6]). The experimental values of the excitation energies $E_x^{\rm exp}$ (see table 1) for the states in ^{19}Na or those known in the mirror nucleus were used. The partial widths are estimated in a standard way from the expression $\Gamma = 2\theta^2\gamma^2 P(\ell,\ Q)$, where Q is the particle decay energy ($Q_p = -320$ keV, $Q = E_x - Q_p$), γ^2 is the Wigner single-particle width and $P(\ell,\ Q)$ is the penetrability, ℓ is the angular momentum of the transition. The penetrabilities are calculated in a Woods-Saxon well using the correct number of nodes of the wave functions. The results of the calculations are shown in table 1 for the states with a total width larger than 5 keV.

No state corresponding to the position of the peaks B and C is present in table 1. A $\frac{1}{2}^-$ state (labelled 4) is positioned at $E_x = 2405$ keV, with a width of 6.1 keV, too narrow to explain the shape of the peaks. The state labelled 5 is positioned close to the peak C. However, the predicted width is again too narrow. In fact, there is no explanation for the two experimental peaks B and C within the framework of the shell model calculations. We have also performed R-matrix calculations using free parameters to simulate the elastic scattering. In no case the calculations fitted the experimental results. In conclusion, the peaks B and C have shapes, positions and intensities that cannot match any interpretation in the frame of elastic scattering.

To study the origin of peaks D and E of fig. 3, we proceeded in an iterative manner. The first two states in ^{19}Na (table 1) are predicted to be too narrow to be observed. The known properties of state 3 in table 1 have been introduced into the R-matrix program to produce an excitation function, which fitted well the peak A. The best-fit parameters for this resonance are reported in table 2. In a second step, we introduced in the R-matrix program the states predicted with width $\Gamma_{\rm gs} > 10$ keV, *i.e.* the three states 7, 8 and 11 of table 1. They all have spin $\frac{3}{2}^-$. Starting from the predicted properties of these states, we have computed an excitation function which was

Table 1. Predicted properties of states in ^{19}Na from shell model calculations. The symbol $E_x^{\rm exp}$ corresponds to the values used to calculate the widths $\Gamma_{\rm gs}$ and Γ_{2^+}. These correspond to the measured values of the excitation energies when known [5,7], or the excitation energies measured in the mirror nucleus ^{19}O [6]; otherwise, the predicted values E_x are used.

Label	J^π	E_x (keV)	$E_x^{\rm exp}$ (keV)	$\Gamma_{\rm gs}$ (keV)	Γ_{2^+} (keV)
1	$\frac{5}{2}^+$	0	0	0.2 eV	0
2	$\frac{3}{2}^+$	293	120	0.6 eV	0
3	$\frac{1}{2}^+$	1467	746	86	0
4	$\frac{1}{2}^-$	2405	–	6.1	0.004
5	$\frac{5}{2}^+$	3167	3153	5.4	367
6	$\frac{3}{2}^+$	3746	3231	2.4	203
7	$\frac{3}{2}^-$	4258	3944	51	0.017
8	$\frac{3}{2}^-$	4667	4582	45	0.080
9	$\frac{1}{2}^-$	4890	–	0.1	29
10	$\frac{5}{2}^+$	5010	–	6.9	216
11	$\frac{3}{2}^-$	5466	–	161	1.3

Table 2. Properties of the peaks measured in ^{19}Na assuming a pure elastic scattering. As the R-matrix calculations cannot fit the peaks B and C, their reported properties are just indicative. See fig. 3 and table 1 for labels.

Labels	J^π	E_x (keV)	$\Gamma_{\rm gs}$ (keV)
A - 3	$\frac{1}{2}^+$	756 ± 18	80 ± 20
B	–	≈ 2.1 MeV	≈ 300 keV
C	–	≈ 2.8 MeV	≈ 500 keV
D - 7	$\frac{3}{2}^-$	4371 ± 10	30 ± 10
E - 8	$\frac{3}{2}^-$	4903 ± 10	50 ± 10

in good agreement with the measurement. It reproduced the peaks D and E when we used the slightly modified properties reported in table 2. The predicted properties for state 11 have been used without modification even though this state may not correspond to single physical state in ^{19}Na. Indeed, at higher energies there is certainly a high density of broad states which are not easy to disentangle.

The final result of the above analysis is plotted in fig. 3 as a continuous line. We can observed a good overall agreement, except for the peaks B and C.

6 Inelastic scattering

The two main observed peaks B and C cannot be explained by the elastic-scattering channel. Nevertheless, the shell model calculations (table 1) have revealed several broad states in the inelastic channel corresponding to the reaction p(^{18}Ne,p$_1$)^{18}Ne*. The use of a thick target does not allow us to separate the inelastic contributions from the elastic scattering. The observed Gaussian shape of the peaks B and C fits with what is expected from inelastic

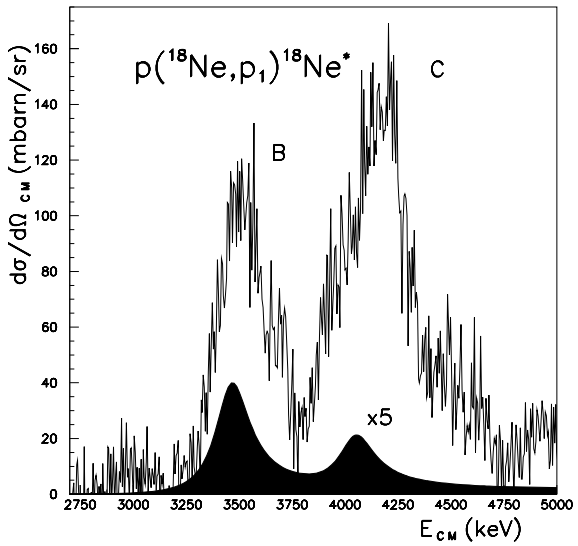

Fig. 4. Peaks B and C from fig. 3 have been re-analyzed in the inelastic-scattering hypothesis. This new result is compared with a R-matrix calculation (the black surface multiplied by a factor of 5) using states 5 and 6 from table 1 with $\Gamma_{\rm gs} = 10$ keV and $\Gamma_{2^+} = 200$ keV. Although the shape and the position of the peaks are in good agreement, the intensities are very different.

scattering. In the hypothesis of an observation of the inelastic scattering, the data has to be re-analyzed to take into account different kinematics and energy losses. A reanalysis of the data has been performed in two steps. First, we have subtracted the calculated elastic excitation function of fig. 3 from the experimental excitation function to reveal possible inelastic contributions. Then, we have re-analyzed this part of the spectrum to produce an excitation function. It resulted in the final experimental histogram shown in fig. 4.

The two peaks B and C are positioned in fig. 4 at energies close to the predicted energies for states 5 and 6. We performed a calculation with the program ANARKI in order to simulate the excitation function for the inelastic scattering. A typical result is shown in fig. 4 (using $\Gamma_{\rm gs} = 10$ keV and $\Gamma_{2^+} = 200$ keV) as a filled surface (multiplied by a factor 5). We observe that the agreement is good for the shape and the position of the peaks, but there is a very large discrepancy in the amplitude. Only a small part of the measured peaks B and C may be due to this inelastic-scattering contribution.

7 Two-proton emission from ^{19}Na

In our experiment several reaction channels are open:

- In the case of ^{18}O: ^{18}O + p (elastic scattering), ^{18}O* + p (inelastic scattering with gamma emission), ^{15}N + α ($Q = +3.98$ MeV), ^{16}O + ^{3}H ($Q = -3.7$ MeV), ^{18}F + n ($Q = -2.44$ MeV), ^{17}O + d ($Q = -5.82$ MeV), ^{14}N + n + α ($Q = -6.85$ MeV), ^{14}C + p + α ($Q = -6.23$ MeV).
- In the case of ^{18}Ne: ^{18}Ne + p (elastic scattering), ^{18}Ne* + p (inelastic scattering with gamma emission), ^{17}F + 2p ($Q = -3.922$ MeV), ^{16}O + 3p ($Q = -4.522$ MeV), ^{14}O + α + p ($Q = -5.113$ MeV).

Several of these inelastic reactions result in the emission of protons, which might produce additional peaks in the excitation function. Therefore, it is important to estimate the intensity of these different inelastic channels. It was done in the following way:

- The silicon telescope allowed a clear identification of the particles with a standard E-ΔE plot. Then it is possible to estimate the intensity of the inelastic channels producing other kinds of particles. In the case of the ^{18}Ne beam we observed only α-particles and β-rays. The α-particles are observed as a very low-intensity contribution and with a continuous energy distribution, in full contrast with the proton energy distribution.
- Several inelastic channels may contribute to the proton production. We have performed several experiments with stable beams (^{18}O, ^{12}C [12], ^{24}Mg [23]) in order to estimate the intensity of the other proton contributions. The very good agreement found in the analysis of the data for the ^{18}O beam is in agreement with the hypothesis that other channels are negligible compared to the elastic scattering. Moreover, no extra peak was visible in the ^{18}O excitation function, even if several reaction channels are open including those with proton emission. In conclusion, in the case of stable beams there was no other important contribution in the excitation function.
- The previous conclusion may not be valid in the case of neutron-deficient beams, where the protons are less bound. In order to clarify this point, we used a silicon strip detector, allowing the detection of particles in coincidence. In the case of the stable ^{18}O beam, no coincidence event was observed. But, in the case of the ^{18}Ne beam, we observed a few hundred events with a proton multiplicity equal to two. Indeed, the probability to detect only one proton after a two-proton emission is much larger than the probability to detect the two protons in coincidence; this means that the two-proton emission channel may induce extra peaks in the elastic-scattering excitation function.

In fig. 5, the individual energies of the two-proton events measured in the present experiment were plotted as a continuous line. This spectrum is compared with that obtained for only one detected proton in the region of the peaks B and C (dashed line), elastic scattering subtracted.

A similar pattern is observed for the two plots, two peaks are present but slightly shifted in energy and with different widths. In fact, the plots correspond to two different selections of the same events. In one case we impose the detection of the two protons, in the other case only one of the two protons is detected, and the differences between the plots are due to correlation and kinematical effects.

To estimate these effects we performed a Monte Carlo simulation of the two-proton emission in a sequential decay mode and with uniform angular distributions in the

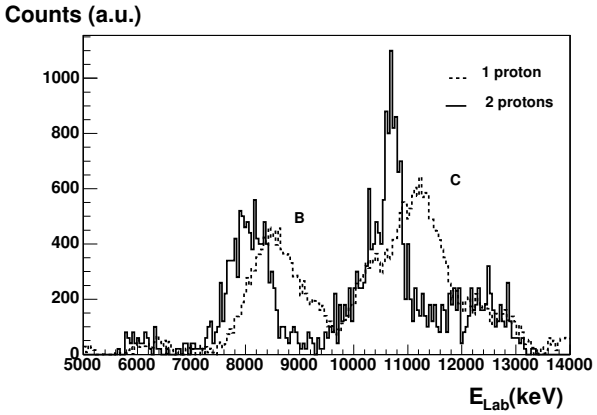

Fig. 5. The individual energies in the laboratory frame of the two-proton events are plotted with a continuous line. The dashed curve represents the spectrum obtained in the region of the peaks B and C, elastic-scattering part subtracted. A similar pattern is observed.

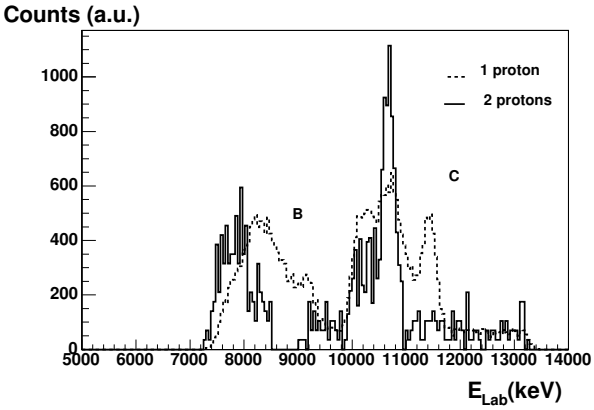

Fig. 6. Monte Carlo simulation of the two-proton decay events using the experimental conditions. The individual energies in the laboratory frame of the detected two-proton events are plotted with a continuous line. The dashed curve represents the spectrum obtained when only one proton is detected. The general pattern is in good agreement with the experimental one of fig. 5.

center-of-mass system. In the simulation, we used the experimental conditions. The parameters used for the two-proton transitions are taken from the analysis described in the next paragraph. Figure 6 shows the results in the same format as fig. 5. One can observe that fig. 6 is similar to fig. 5. We found that the selection produces an energy shift in agreement with the experimental observation. The broadening of peak C in fig. 6 is not in agreement with the data of fig. 5. The exact shape of the peak depends strongly on the correlation function, *i.e.* the angular distributions may not be uniform. Moreover, the factor corresponding to the ratio between the number of one-proton events divided by the number of two-proton events, has been found to be equal to 67 in the simulation, close to the experimental value of 81 ± 8 which corresponds to the ratio between the number of protons measured in the two peaks B and C, divided by the total number of protons detected in coincidence.

The above analysis shows that the two peaks B and C result from the detection of only one proton from a complex combination of several two-proton emissions.

8 Analysis of the two-proton events

The analysis of the two-proton events can be performed assuming a sequential two-proton emission, *i.e.* the 2 protons are emitted one after another from an initial state in the compound nucleus ^{19}Na, through an intermediate state in ^{18}Ne. This problem has an infinite number of solutions because one starts with the two measured energies for the transitions in order to deduce 3 excitation energies: the initial state in ^{19}Na, the intermediate state in ^{18}Ne, and the final state in ^{17}F. To obtain a solution we have to assign the final state of ^{17}F in the initial conditions. However, this problem still has two solutions, because one does not know which proton has been emitted first. An example of an ensemble of solutions is shown in fig. 7 in

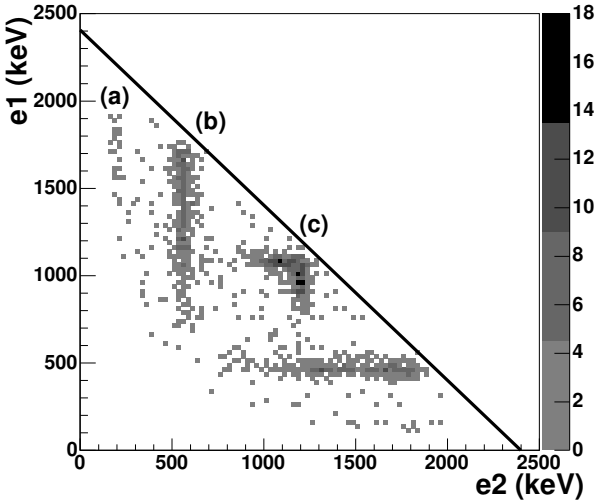

Fig. 7. The reconstructed two-dimensional energy distribution of the experimental two-proton events. The y-axis corresponds to the center-of-mass energy of the first transition, from one excited state in ^{19}Na to one excited state in ^{18}Ne, the x-axis is the energy of the second transition from the state in ^{18}Ne to ^{17}F$_{gs}$. The continuous line corresponds to the maximum energy available in the center-of-mass system. The 3 clusters of events producing the vertical lines labelled (a), (b) and (c), correspond to sequential transitions (see text).

the case where the final state is the ground state of ^{17}F. The energy $e1$ of the first transition is plotted *versus* the energy $e2$ of the second transition in center-of-mass frame. It is very important to observe that the points are aligned along straight horizontal and vertical lines, thus providing a hint for a sequential decay. Indeed, the kinematical and energy loss corrections between the detected energies and the center-of-mass energies are so strong, that this observation constitutes a confirmation of the interpretation of

Table 3. Results corresponding to the two-proton events analyzed in the sequential mode. The widths Γ_{e1} and Γ_{e2} refer to the widths of the proton transitions, and Γ to the widths of the excited states.

Label	$e1(^{19}\mathrm{Na} \rightarrow {}^{18}\mathrm{Ne})$ (keV)	Γ_{e1} (keV)	$E_x(^{19}\mathrm{Na})$ (keV)	$\Gamma(^{19}\mathrm{Na})$ (keV)	$e2(^{18}\mathrm{Ne} \rightarrow {}^{17}\mathrm{F}_{\mathrm{gs}})$ (keV)	Γ_{e2} (keV)	$E_x(^{18}\mathrm{Ne})$ (keV)	$\Gamma(^{18}\mathrm{Ne})$ (keV)
(a)	1698 ± 75	541 ± 178	5499 ± 76	539 ± 180	200 ± 12	40 ± 34	4121 ± 12	9^{+54}_{-9}
(b)	1424 ± 30	697 ± 72	5585 ± 32	695 ± 72	560 ± 11	47 ± 4	4481 ± 11	27^{+6}_{-9}
(c)	1018 ± 13	154 ± 17	5815 ± 17	141 ± 18	1196 ± 11	51 ± 6	5117 ± 11	33^{+9}_{-11}
					$e2(^{18}\mathrm{Ne} \rightarrow {}^{17}\mathrm{F}_{p1})$			
(a*)	1557 ± 66	463 ± 215	5809 ± 76	460 ± 215	156 ± 12	39 ± 15	4572 ± 12	0^{+37}_{-0}

the data. This also means that the assumption of the $^{17}\mathrm{F}_{\mathrm{gs}}$ as the final state is a realistic hypothesis. The widths of the lines correspond to widths of the transitions Γ_{e1} and Γ_{e2}. The final interpretation is made after checking two conditions. The maximum energy available in the center of mass is limited by the beam energy. The width of the first transition is a convolution of the width of the initial state and the width of the intermediate state. This means the first transition has always to be broader than the second one. This second condition also means we have to select vertical lines in the plot.

In fig. 7 we can observe 3 independent vertical clusters of points labelled (a), (b) and (c). The analysis of the plot has been performed using the Breit-Wigner formula for the shape of the states. The maximum energy available in the center of mass is indicated by the line $e1 + e2 = 2400$ keV in this figure. Some events are very close to that limit, which may indicate that a part of the resonance is not observed. In the analysis, an energy limit has been introduced to take into account this effect. The energy resolution is estimated to be about 40 keV. The total widths Γ of the states have been determined taking into account this energy resolution. The results of this analysis are summarized in table 3.

Moreover, the first-excited state in ^{17}F is only 495 keV above the ground state. Hence, we have also to consider the decay to this final state. In this hypothesis there is not enough energy left in the center-of-mass frame to interpret a large part of the events seen in the transitions (b) and (c) of fig. 7. On the other hand, all the events of the transition (a) can be analyzed in this hypothesis. The results are summarized in the last row of table 3 and labelled (a*).

As a final check we have compared our measured states in ^{18}Ne with the known properties of the excited states in that nucleus. The state determined from transition (a) in the first row of table 3 is not known, the closest states in ^{18}Ne are a 1^- state positioned 399 keV above our measured state, at $E_x = 4520 \pm 7$ keV [24], and a 2^+ state positioned 505 keV below, at $E_x = 3616.4 \pm 0.6$ keV [25]. On the contrary, a correspondence can be found within the error bars in the (a*) case of table 3. There is a known state at $E_x = 4589 \pm 7$ keV, with $J^\pi = 0^+$ [25], which gives a difference in energy of $+17 \pm 19$ keV. There are two other known states at $E_x = 4523.7 \pm 2.7$ keV, with $J^\pi = 3^+$ [11], and at $E_x = 4520 \pm 7$ keV, with $J^\pi = 1^-$ [25], which give

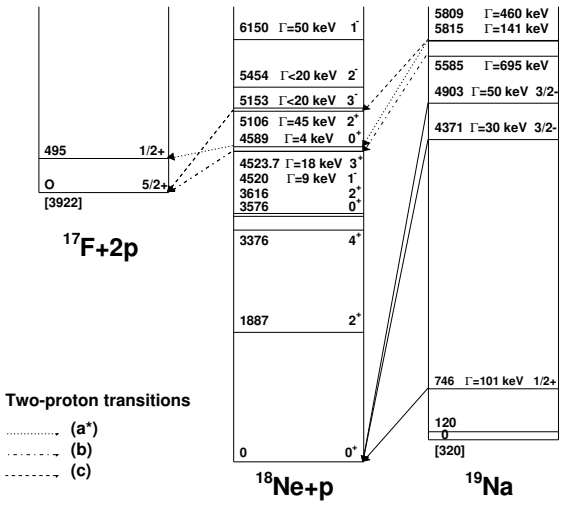

Fig. 8. Level scheme which summarizes the known-states properties of ^{19}Na. All known states on ^{18}Ne are also shown up to 6.2 MeV. The observed two-proton transitions are shown with dashed lines. They are all connected with known states in ^{18}Ne above the proton emission threshold.

an energy difference of -48.3 ± 14.7 keV and -52 ± 19 keV. Our measured width $\Gamma = 0\ ^{+37}_{-0}$ keV is also in agreement with the known values $\Gamma = 4 \pm 4$ keV, $\Gamma = 18 \pm 3$ keV and $\Gamma = 9 \pm 6$ keV. In the 0^+ state hypothesis, the proton may decay to the ground state of ^{17}F ($J^\pi = \frac{5}{2}^+$) or to the first-excited state at $E_x = 495$ keV ($J^\pi = \frac{1}{2}^+$). In the first case, the transition has $\ell = 2$, and for the second case $\ell = 0$. The lower angular-momentum barrier may explain why we observe the transition to the first-excited state.

The state determined from the transition (b) can be associated with two states in ^{18}Ne: the state at $E_x = 4520 \pm 7$ keV, $J^\pi = 1^-$, or the state at $E_x = 4523.7 \pm 2.9$ keV, $J^\pi = 3^+$. In these cases we found a difference in energies of 39 ± 18 keV and of 43 ± 14 keV, respectively.

The state determined from the transition (c) can be associated with two states: $E_x = 5153 \pm 8$ keV with $\Gamma \leq 20$ keV and $J^\pi = 3^-$ [24], and $E_x = 5106 \pm 8$ keV with $\Gamma = 45 \pm 2$ keV and $J^\pi = 2^+$ [26]. The difference in energies is equal to $+36 \pm 19$ keV and -11 ± 19 keV.

The final overview of the results is presented in fig. 8. All known states in ^{18}Ne are shown up to 1.5 MeV above the proton emission threshold. The observed two-proton transitions are shown as dashed lines. It is interesting to observe that all transition lines are connected with known states in ^{18}Ne, and, inversely, all known states above the proton emission threshold have been fed by a two-proton emission. Two states in ^{19}Na at 5809 keV and 5815 keV may be related to one unique state. In the mirror nucleus ^{19}O there are several states known at close energies, two of them may be the analogue states since they have large widths: $\Gamma = 490$ keV at $E_x = 5.54$ MeV with $J^\pi = \frac{3}{2}^+$, and $\Gamma = 110$ keV at $E_x = 6.120$ MeV with $J^\pi = \frac{3}{2}^+$. However, it is probable that the states determined in ^{19}Na from the two-proton emission result from the mixed combination of several broad states. In such a hypothesis, the two-proton emission occurs up to the maximum energy available in the center-of-mass frame, which seems to be the case here.

As discussed above, in fig. 3 the peaks B and C correspond to the detection of only one proton of the two-proton emissions. The efficiency to detect such events at forward angles is increased in inverse kinematics. The focusing effects also exist in inelastic scattering followed by gamma emission. An example of (p, pγ) contribution has been shown in fig. 4 for the inelastic scattering on the first-excited state. Calculations show that the focusing effect is higher when the total available energy is shared by two protons. This explains why we observe only the peaks B and C, corresponding to two-proton decays (p, pp), and not other peaks corresponding to inelastic (p, pγ) contributions. However, these inelastic contributions should be present in fig. 3 with a lower amplitude than the elastic scattering, and they may explain the small differences we can observe between the R-matrix calculation and the experimental data.

In fig. 7, it is surprising to observe that the transition labelled (c) is located near $e1 = e2$. For these events, the difference in energy is very small, the mean value is $|\overline{e1 - e2}|_{\rm lab} = 500 \pm 370$ keV and at the same time the sum is $|\overline{e1 + e2}|_{\rm lab} = 21200 \pm 510$ keV. These events may be related to the simultaneous emission of two protons (^{2}He emission). The equality of the energies may be a natural consequence of this decay mode. Gómez del Campo *et al.* [26] have observed such events in ^{18}Ne, *i.e.* a clear evidence for the simultaneous emission from the 6.15 MeV state ($J^\pi = 1^-$). Since the three-proton emission channel is open in our case, the events labelled (c) may be related to this emission mode. No event with 3 protons in coincidence has been observed, but the detection efficiency is very low for this kind of events. The probability to observe 2 of the 3 protons is much larger.

The simulation of this process (using the sequential emission model as described above) has shown that we do not have enough energy in the center-of-mass frame to produce 3-proton emission where two of them correspond to the observed two-proton events. In conclusion, no three-proton emission was observed in our experiment. As we have seen, the analysis of these events (c), using the model of a sequential two-proton emission, involves an intermediate excited state in ^{18}Ne. This state was already known before our experiment. It is probable that the equality of the energies is purely accidental.

9 Conclusions

We have performed an experiment to measure the elastic-scattering excitation function of a ^{18}Ne radioactive beam from the SPIRAL facility on a thick solid cryogenic hydrogen target. Two new states in the compound nucleus ^{19}Na with $J^\pi = \frac{3}{2}^-$, at $E_x = 4371 \pm 10$ keV with $\Gamma = 30 \pm 10$ keV and at $E_x = 4903 \pm 10$ KeV with $\Gamma = 50 \pm 10$ keV were observed. The understanding of the decay process was crucial to understand the high-energy part of the ^{19}Na excitation function. Two intense peaks mainly correspond to the detection of single protons from two-proton emissions. It is important to point out that the detection efficiency of two-proton events is enhanced at forward angles in inverse kinematics. The two-proton events have been interpreted to arise from a sequential decay, and three new states with large width have been determined in ^{19}Na.

Future experiments of elastic scattering at low energy will provide an efficient way to undertake the spectroscopy of nuclei close to the drip lines. These future experiments aimed at the search for states at high excitation energies in the unbound neutron-deficient nuclei should take into account the detection of the multi-proton events and include proton detectors of high granularity and energy resolution. In addition, the improvement of the detection system by increasing the total acceptance and by measuring the angular distribution will allow the efficient spectroscopy of the intermediate states from multi-particle emissions. However, it is important that future theoretical studies shed light on the two-proton emission from excited states, and particularly on the simultaneous-emission mode.

We would like to thank the GANIL staff and the technical support for the successful challenge of providing for the first time the SPIRAL beam. We are grateful to Dr M. Ploszajczak and Dr N. Alahari for stimulating discussions. This work has been supported by the European Community-Access to Research Infrastructure action of the Improving Human Potential Program, contract No. HPRI1999-00066.

References

1. M. Notani, H. Sakurai, N. Aoi, Y. Yanagisawa, A. Saito, N. Imai, T. Gomi, M. Miura, S. Michimasa, H. Iwasaki, N. Fukuda, M. Ishihara, T. Kubo, S. Kubono, H. Kumagai, S.M. Lukyanov, T.K. Onishi, Yu.E. Penionzhkevich, S. Shimoura, T. Teranishi, K. Ue, V. Ugryumov, A. Yoshida, Phys. Lett. B **542**, 49 (2002).
2. S.M. Lukyanov, Yu.E. Penionzhkevich, R. Astabatyan, S. Lobastov, Yu. Sobolev, D. Guillemaud-Mueller, G. Faivre, F. Ibrahim, A.C. Mueller, F. Pougheon, O. Perru, O. Sorlin, I. Matea, R. Anne, C. Cauvin, R. Hue, G. Georgiev, M. Lewitowicz, F. de Oliveira Santos, D. Verney, Z. Dlouhy, J. Mrazek, D. Baiborodin, F. Negoita, C. Borcea, A. Buta, I. Stefan, S. Grevy, J. Phys. G. **28**, L41 (2002).

3. T. Zerguerras, B. Blank, Y. Blumenfeld, T. Suomijrvi, D. Beaumel, B.A. Brown, M. Chartier, M. Fallot, J. Giovinazzo, C. Jouanne, V. Lapoux, I. Lhenry-Yvon, W. Mittig, P. Roussel-Chomaz, H. Savajols, J.A. Scarpaci, A. Shrivastava, M. Thoennessen, Eur. Phys. J. A **20**, 389 (2004).
4. J. Cerny, R.A. Mendelson, G.J. Wozniak, J.E. Esterl, J.C. Hardy, Phys. Rev. Lett. **22**, 612 (1969).
5. W. Benenson, A. Guichard, E. Kashy, D. Mueller, H. Nann, L.W. Robinson, Phys. Lett. B **58**, 46 (1975).
6. D.R. Tilley, H.R. Weller, C.M. Cheves, R.M. Chasteler, Nucl. Phys. A **595**, 1 (1995).
7. C. Angulo, G. Tabacaru, M. Couder, M. Gaelens, P. Leleux, A. Ninane, F. Vanderbist, T. Davinson, P.J. Woods, J.S. Schweitzer, N.L. Achouri, J.C. Angélique, E. Berthoumieux, F. de Oliveira Santos, P. Himpe, P. Descouvemont, Phys. Rev. C **67**, 014308 (2003).
8. C. Angulo, M. Azzouz, P. Descouvemont, G. Tabacaru, D. Baye, M. Cogneau, M. Couder, T. Davinson, A. Di Pietro, P. Figuera, M. Gaelens, P. Leleux, M. Loiselet, A. Ninane, F. de Oliveira Santos, R.G. Pizzone, G. Ryckewaert, N. de Séréville, F. Vanderbist, Nucl. Phys. A **716**, 211 (2003).
9. R. Coszach, M. Cogneau, C.R. Bain, F. Binon, T. Davinson, P. Decrock, Th. Delbar, M. Gaelens, W. Galster, J. Goerres, J.S. Graulich, R. Irvine, D. Labar, P. Leleux, M. Loiselet, C. Michotte, R. Neal, G. Ryckewaert, A.S. Shotter, J. Vanhorenbeeck, J. Vervier, M. Wiescher, Ph. Woods, Phys. Lett. B **353**, 184 (1995).
10. J.-S. Graulich, R. Coszach, P. Leleux, Eur. Phys. J. A **13**, 221 (2002).
11. D.W. Bardayan, J.C. Blackmon, C.R. Brune, A.E. Champagne, A.A. Chen, J.M. Cox, T. Davinson, V.Y. Hansper, M.A. Hofstee, B.A. Johnson, R.L. Kozub, Z. Ma1, P.D. Parker, D.E. Pierce, M.T. Rabban, A.C. Shotter, M.S. Smith, K.B. Swartz, D.W. Visser, P.J. Woods, Phys. Rev. Lett. **83**, 45 (1999).
12. L. Axelsson, M.J.G. Borge, S. Fayans, V.Z. Goldberg, S. Grevy, D. Guillemaud-Mueller, B. Jonson, K.-M. Kallman, T. Lonnroth, M. Lewitowicz, P. Manngård, K. Markenroth, I. Martel, A.C. Mueller, I. Mukha, T. Nilsson, G. Nyman, N.A. Orr, K. Riisager, G.V. Rogatchev, M.-G. Saint-Laurent, I.N. Serikov, O. Sorlin, O. Tengblad, F. Wenander, J.S. Winfield, R. Wolski, Phys. Rev. C **54**, R1511 (1996).
13. V.Z. Goldberg, V.I. Dukhanov, A.E. Pakhomov, G.V. Rogachev, I.N. Serikov, M. Brenner, K-M. Källman, T. Lönnroth, P. Manngård, L. Axelsson, K. Markenroth, W. Trzaska, R. Wolski, Phys. At. Nucl. **60**, 1061 (1997), (Yad. Fiz. **60**, 1186 (1997)).
14. K. Markenroth, L. Axelsson, S. Baxter, M.J.G. Borge, C. Donzaud, S. Fayans, H.O.U. Fynbo, V.Z. Golberg, S. Grévy, D. Guillemaud-Mueller, B. Jonson, K.-M. Källman, S. Leenhardt, M. Lewitowicz, T. Lönnroth, P. Manngard, I. Martel, A.C. Mueller, I. Mukha, T. Nilsson, G. Nyman, N.A. Orr, K. Riisager, G.V. Rogatev, M.-G. Saint-Laurent, I.N. Serkov, N.B. Shul'gina, O. Sorlin, M. Steiner, O. Tengblad, M. Thoennessen, E. Tryggestad, W.H. Trzaska, F. Wenander, J.S. Winfield, R. Wolski, Phys. Rev. C **62**, 034308 (2000).
15. A.C.C. Villari, C. Barue, G. Gaubert, S. Gibouin, Y. Huguet, P. Jardin, S. Kandri Rody, F. Landre Pellemoine, N. Lecesne, R. Leroy, M. Lewitowicz, C. Marry, L. Maunoury, J.Y. Pacquet, J.P. Rataud, M.G. Saint-Laurent, C. Stodel, J.C. Angelique, N.A. Orr, R. Lichtenthaler, Nucl. Phys. A **701**, 476c (2002).
16. A.C.C. Villari, the SPIRAL group, Nucl. Instrum. Methods B **204**, 31 (2003).
17. W. Mittig, P. Roussel-Chomaz, Nucl. Phys. A **693**, 495 (2001).
18. J.F. Ziegler, J.P. Biersack, U. Littmark, *The Stopping and Range of Ions in Solids* (Pergamon Press, New York, 1985) (2003) and `http://www.srim.org/`.
19. H. Orihara, G. Rudolf, Ph. Gorodetzky, Nucl. Phys. A **203**, 78 (1973).
20. E. Berthoumieux, B. Berthier, C. Moreau, J.P. Gallien, A.C. Raoux, Nucl. Instrum. Methods B **136-138**, 55 (1998).
21. E.K. Warburton, B.A. Brown, Phys. Rev. C **46**, 923 (1992).
22. B.A. Brown, A. Etchegoyen, W.D.M. Rae, MSU-NSCL report No. 524, 1986, unpublished.
23. Achouri Nadia Lynda, PhD manuscript, Université de Caen/Basse Normandie (2001).
24. K.I. Hahn, A. Garcia, E.G. Adelberger, P.V. Magnus, A.D. Bacher, N. Bateman, G.P.A. Berg, J.C. Blackmon, A.E. Champagne, B. Davis, A.J. Howard, J. Liu, B. Lund, Z.Q. Mao, D.M. Markoff, P.D. Parker, M.S. Smith, E.J. Stephenson, K.B. Swartz, S. Utku, R.B. Vogelaar, K. Yildiz, Phys. Rev. C **54**, 1999 (1996).
25. A. Garcia, E.G. Adelberger, P.V. Magnus, D.M. Markoff, K.B. Swartz, M.S. Smith, K.I. Hahn, N. Bateman, P.D. Parker, Phys. Rev. C **43**, 2012 (1991).
26. J. Gómez del Campo, A. Galindo-Uribarri, J.R. Beene, C.J. Gross, J.F. Liang, M.L. Halbert, D.W. Stracener, D. Shapira, R.L. Varner, E. Chavez-Lomeli, M.E. Ortiz, Phys. Rev. Lett. **86**, 43 (2001).